Effects of Aerothermal Shape Distortion on Hypersonic Vehicle Performance in Cruise

L. Pollock[1], J. Moran[2] and A. Neely[3]
University of New South Wales, Canberra, ACT, 2612, Australia

This paper explores the effects of aerothermal shape distortion upon the aerodynamic performance of a hypersonic vehicle. A reference waverider vehicle was designed to operate at a nominal cruise condition of Mach 7 at 39 km altitude. A simple semi-monocoque structure made from titanium alloy skins and frames is used with constant skin thicknesses and a solid tungsten nose ballast. The aerodynamic performance of the vehicle was assessed using Ansys Fluent with the Spalart-Allmaras turbulence model. Multiphysics aerothermal distortion was computed using a two-way steady state coupled approach with linearly interpolated temperatures. This resulted in an increase in maximum drag of 14.8% and a decrease in the maximum lift-to-drag ratio of 4.76%. Significant changes in the stability of the vehicle were also observed at higher angles of attack.

I. Nomenclature

C_L	=	lift coefficient
C_D	=	drag coefficient
C_{D0}	=	profile coefficient
K	=	lift induced drag coefficient
$C_{M_{CG}}$	=	pitching moment coefficient at the center-of-gravity
C_P	=	pressure coefficient
$C_{P_{max}}$	=	maximum pressure coefficient on the vehicle
γ	=	heat capacity ratio
M_∞	=	freestream Mach number
θ	=	local inclination to the freestream
$(C_x)_d$	=	change in an aerodynamic coefficient because of aerothermal distortion (example)

II. Introduction

Hypersonic vehicles (HSVs) – those that are typically classified as designed to fly at over five times the speed of sound (Mach 5) – operate at extreme speeds and present novel applications, both military and civil [1]. Civil applications have been proposed for rapid point-to-point travel or access to space via runway [2, 3]. Hypersonic space access vehicles often blur the line between traditional designs and have merited their own designation – spaceplanes – that may take off and land on a conventional runway but also permit space access. Military HSVs can be employed to target a time-critical threat or employ their extreme speed to avoid conventional ballistic countermeasures [4]. Regardless of the application, HSVs face novel engineering challenges that have limited their application to sparse scientific endeavors.

---

[1] Research Associate, School of Engineering & Information Technology, AIAA Member.
[2] Research Associate (Hypersonics), AIAA Member. Currently at the University of Southern Queensland, Institute for Advanced Engineering and Space Sciences.
[3] Associate Dean of Research Engagement, Professor, School of Engineering & Information Technology, AIAA Associate Fellow.

A. Hypersonic Vehicle Design

The extreme energies associated with flight at hypersonic conditions make it difficult to mimic this flight in ground test facilities. Hypersonic wind tunnels are sparsely available, yet growing in number, and often only replicate a subset of hypersonic flow conditions. Shock tunnels simulate high enthalpy conditions for extremely short durations (typically < 10 ms) [5] whilst blowdown tunnels can create long duration or continuous test times at low enthalpies [6]. Arc jet facilities can create extremely high enthalpy flows but are not very well suited for aerodynamic testing and are hence usually limited to the study of high-temperature materials [7].

The potential for a flight test, whilst capable of replicating all flow conditions, presents with exceedingly higher risk and cost. HSV flight experiments have almost exclusively been employed for scientific study and have traditionally only been commissioned for a sparse number of tests [8, 9]. The high cost and risk of a flight test coupled with the long project durations required to prepare them results in them usually being avoided in preference for cheaper and safer ground tests. Alternative approaches to HSV flight tests including balloon testing and reusable vehicles, can decrease costs and can make flight tests a more economical option for scientific study. Investment from industry into hypersonic flight will inevitably drive down prices and make flight tests a more feasible option for the scientific community.

As a result of these challenges, hypersonic designers typically resort to extensive use of numerical modelling. Numerical methods still face limitations but are being continuously developed as a means of overcoming the constraints of physical testing. Computational fluid dynamic (CFD) codes for hypersonic flow span over a wide range of development from experimental through to commercial. Likewise, the level of fidelity can vary widely, depending upon the goals of the code from direct numerical simulations (DNS) that capture all the Kolmogorov scales and can take tens of thousands of computing hours through to inviscid panel methods that may take a laptop microseconds to resolve. The development of a numerical wind tunnel that is accurate enough to replicate results of a physical wind tunnel experiment and can solve in the same timeframe is a desirable goal to eliminate ground testing almost entirely [10].

Ultimately, the design of a HSV will be evaluated over numerous levels of testing including both physical and numerical. From a numerical perspective, a multi-fidelity approach is typically adopted wherein the level of fidelity is tailored to the case. DNS is far too expensive to determine the entire external aerodynamics of a vehicle and is almost always unnecessary. Likewise, an inviscid panel method is completely incapable of predicting the turbulence, chemistry, mixing, and heating that occurs inside a propulsion system. In more recent years, surrogate models have been developed that attempt to leverage developments in artificial intelligence to develop a data-driven model from a multifidelity dataset [11-13].

B. Aerothermal Shape Distortion

A design consideration that is present for all high-speed but most significant for HSVs is that of aerothermal shape distortion [14]. In the hypersonic regime, the extreme heating results in a loss of structural rigidity which when coupled with the pressure loads on the vehicle results in deformation to the structure. In addition, differential thermal expansion will induce internal stresses and can buckle the structure. This deformation can be entirely elastic in which the vehicle would return to its original shape after a flight but is still critical during operation. Aerothermal distortion of a HSV can result in numerous undesirable, and potentially deleterious and even catastrophic effects, as listed below:

- A reduction in aerodynamic efficiency [15],
- Changes to stability – a 10% change in aerodynamic forces results in a 34% change in short-period frequency [16],
- Loss of structural integrity [17],
- Decreased structural life [18],
- Decrease in control authority [19],
- Flow path problems (unstart, loss in efficiency, etc.) [20, 21] and,
- Potentially new aerodynamic phenomena such as SBLI [22, 23].

Aerothermal shape distortion is a particularly challenging design feature to model. From a physical perspective, both a high enthalpy and long duration flow is typically required to accurately replicate the vehicle heating in a ground-based experiment. A short duration but high enthalpy facility does not have the required runtime to permit the thermal soak of the structure. Alternatively, the structure can be thermally soaked from an external source prior to the tunnel run. This method has proven useful for the analysis of fluid-thermal-structural interaction (FTSI) on a more fundamental level, such as for constituent geometries [24, 25]. When considering the effects on an entire vehicle, it is extremely challenging to replicate the high, nonuniform thermal distributions across the geometry and scales required.

Numerical modelling of shape distortion is also challenging, but often less costly than its physical counterpart. In this case, multiple codes must be coupled together through several possible methods to capture all underlying physics. For example, the flow must be solved with a CFD solver whilst the heating of the structure requires a thermal solver and deformation requires a structural solver. These three solvers must be capable of communicating information to each other over boundary conditions, a feature that is not common. More generalized commercial software packages that are used to solve industrial problems are beginning to incorporate this form of multiphysics coupling as an additional level of fidelity. In this work, the Ansys software package has been used to model the aerothermal shape distortion of a HSV and will be discussed further in subsequent sections.

C. Reference Vehicle

A reference HSV has been designed as a generic test bed for assessing the effects of aerothermal shape distortion. The vehicle is a viscous optimized waverider suited for a boost-glide style trajectory, incorporating no internal flow path for a propulsive system. A waverider geometry endeavors to improve lift-to-drag performance by creating an overpressure on the windward (underside) of the vehicle through the formation of shockwaves from the leading edge, thereby generating compression lift.

The complexity of modelling a propulsive system has not been considered at this stage and instead the effect of aerothermal structural deformation on flow path distortion [ref 22 here] is potential future work to be completed. The lack of a propulsive system reduces the vehicle to a boost-glide trajectory wherein it is assisted by means of a booster to a designated altitude and released. The vehicle then glides along its flightpath to its designated destination. These types of vehicles can also incorporate a variety of skipping maneuvers, moving through different layers of density in the atmosphere to increase their range, akin to a stone skipping along the surface of a body of water [26, 27].

The reference HSV outer mold line (OML) for this work was based off a viscous optimized waverider by Moran, et al. [28]. Maximum lift-to-drag and volumetric efficiency for cruise at Mach 7 and an altitude of 39 km were utilized as optimizer targets. These targets are notionally consistent with other flight tests in literature [29].

III. Numerical Methodology

In this initial phase of work, the effects of aerothermal shape distortion upon the reference vehicle have been assessed at its steady-state cruise condition. Atmospheric properties of this condition are given in Table 1 below and are determined from the US Standard Atmosphere 1976 [30]. The vehicle has been modeled from +15° to -15° angle-of-attack (AoA) with an assessment of motion constrained about the longitudinal plane, i.e., to only three degrees of freedom (3DOF) – lift, drag, and pitch. The vehicle is shown in Figure 1 below.

Table 1. The cruising atmospheric test conditions at 39 km altitude.

Altitude (km)	Mach Number	Velocity (m/s)	Density (kg/m^3)	Temperature (K)	Pressure (Pa)	Unit Reynolds Number (m^{-1})
39	7	2207	4.627×10^{-3}	247.6	328.8	5.707×10^{5}

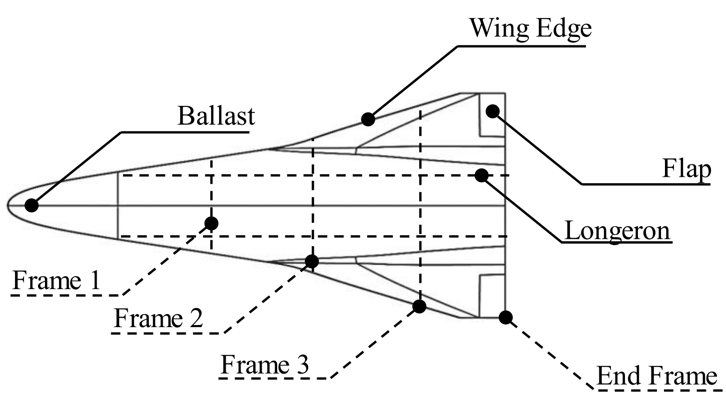

Figure 1. The generic reference hypersonic vehicle designed to cruise at Mach 7.

The vehicle is constructed from a generic titanium alloy with skin and frame thicknesses of 1 mm and 2 mm, respectively to form a simplified structure. The good mechanical performance of titanium at moderately high temperatures makes it suitable for the lower-hypersonic regime. The ballast of the vehicle is composed of tungsten due to its high density which acts to balance the center-of-gravity (CoG) and move it forward to ensure longitudinal stability. The structure of the vehicle can be considered under-designed and acts as a suitable test case to ensure that aerothermal shape distortion is observable. Mechanical and physical properties of the materials used in computational modelling are given in Table 2 below. A linear relationship between stiffness and temperature is assumed for the study.

Table 2. Material properties of the titanium alloy and tungsten used in simulations.

	Young's Modulus (GPa)	Density (kg/m^3)	Poisson's Ratio	Thermal Conductivity (W/m K)	Specific Heat Capacity (J/kg K)
Titanium Alloy	96	4620	0.38	7.44	544
Tungsten	430	19300	0.28	120	150

A. Reynold's Averaged Navier-Stokes (RANS) Method

Viscous simulations have been performed using the Spalart-Allmaras (SA), one-equation turbulence model. The SA turbulence model has been extensively used and validated in the literature for attached hypersonic external aerodynamics and can accurately predict wall heat fluxes with a typical mesh y+ value less than three [31-33]. A half-symmetry, poly-hexcore mesh using mosaic meshing technology has been generated within Fluent. This type of mesh constructs a cartesian hexcore mesh in the bulk of the domain with polyhedral elements used to transition between boundaries. The resulting mesh is highly adaptable to complex geometries whilst retaining some of the advantages of a structured hexahedral domain, including the ability to be generated very rapidly. Examples of the mesh are shown in Figure 2.

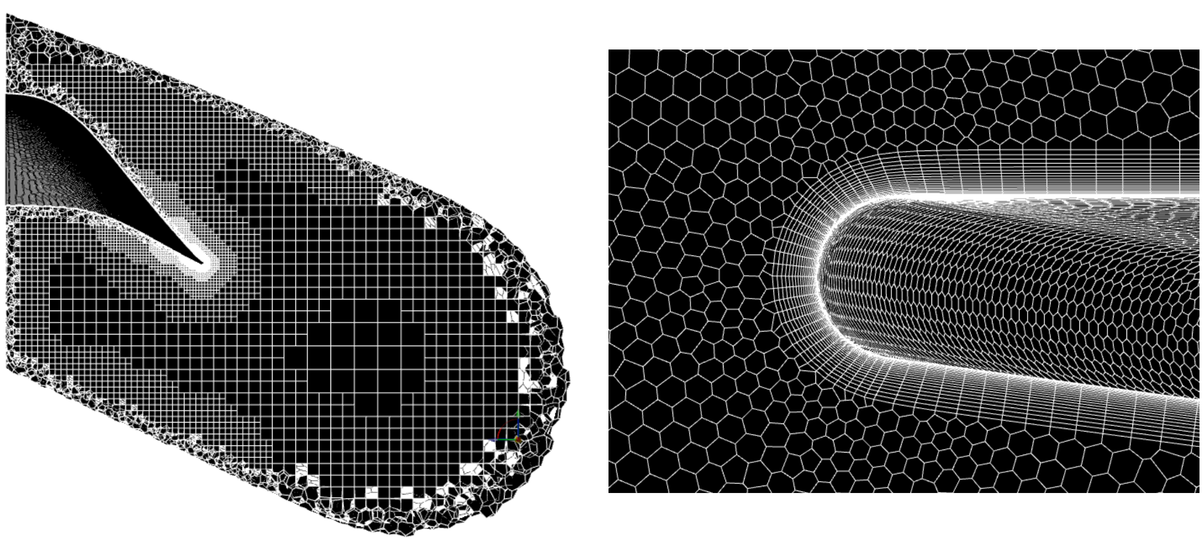

Figure 2. An example of the poly-hexcore mesh used for a cross-section (left) and the inflation layer around the body (right).

The mesh was constructed to fit close to the body whilst allowing all shocks to pass through the outlet at the rear of the domain. A farfield pressure boundary condition was applied on all other surfaces with the values given in Table 1. A schematic of the full domain is shown below.

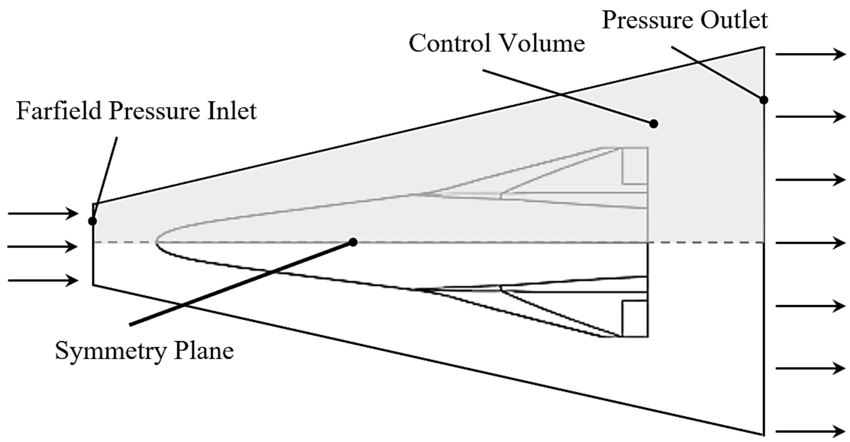

Figure 3. A diagram of the computational domain.

Whilst density-based solvers are typically employed for high-speed flows, the pressure-based solver within Fluent has exhibited excellent robustness and good correlations with experimental data in cases without high-temperature gas effects [28, 34, 35]. Hence, in an engineering context, the pressure-based solver has proved superior for rapidly generating external aerodynamic databases. The setup for the solver is given below in Table 3. In all cases, the ideal-gas law was used to model compressibility. A pseudo-transient time-stepping approach was used to achieve the steady-state solution. The case was considered converged when the residuals for lift, drag, and moment fell below 10^{-3}.

Table 3. Pressure-based solver properties for all computations.

Solver	Pressure-based
Scheme	Coupled
Flux-type	Momentum weighted
Spatial Discretization	
Gradients	Least squares cell based
Pressure	2nd Order
Density	3rd Order MUSCL
Momentum	3rd Order MUSCL
Modified Turbulent Viscosity	3rd Order MUSCL
Energy	3rd Order MUSCL

Aerodynamic databases were generated both by considering constant values for specific heat capacity, viscosity, and thermal conductivity as well as piecewise-linear (PWL) interpolations from experimental data taken from Incropera, et al. [36]. It was ultimately shown that the additional level of fidelity from using PWL interpolations was unnecessary as it provided negligible changes to the aerodynamic properties of the vehicle. Moreover, a noted reduction in the level of robustness was observed when using PWL data. Whilst PWL values are likely to become more important at higher Mach numbers and lower altitudes, due to higher temperatures, the added level of complexity was deemed unnecessary for this work and constant values were assumed for all further calculations.

B. Modified Newtonian Method

As an alternative to viscous CFD, aerodynamic performance was also evaluated using an inviscid panel method, incorporated within an in-house port of the Supersonic/Hypersonic Arbitrary Body Program (S/HABP). S/HABP has the capability to rapidly evaluate the inviscid aerodynamic properties of an arbitrary body by reading in a triangulated mesh (STL file) and applying any number of possible numerical methodologies. In this case, the modified Newtonian (MN) method was applied to calculate aerodynamic data and compare with viscous results. The MN method is part of a class of local surface inclination methods with the capability to rapidly evaluate aerodynamic performance. Such methods have been extensively applied for the preliminary optimization of supersonic and hypersonic bodies. The

MN method is based upon the idea that aerodynamic forces are the result of momentum changes from a stream of fluid being diverted tangentially to a surface.

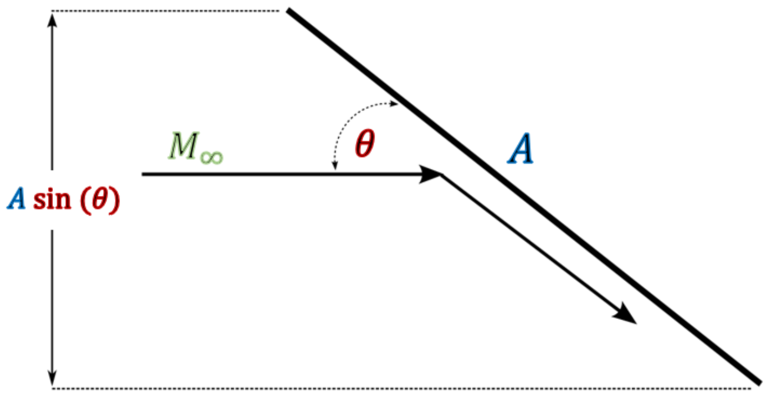

Figure 4. The general concept for local surface inclination methods.

The resulting analysis of momentum transfer produces a simple relationship.

$$C_P = C_{P_{max}} \sin^2 \theta$$

Where,

$$C_{P_{max}} = \frac{2}{\gamma M_\infty^2}\left\{\left[\frac{(\gamma+1)^2 M_\infty^2}{4\gamma M_\infty^2 - 2(\gamma-1)}\right]^{\gamma/\gamma-1}\left[\frac{1-\gamma+2\gamma M_\infty^2}{\gamma+1}\right]-1\right\}$$

Or in the case where it is assumed $M_\infty \to \infty$,

$$C_{P_{max}} = \left[\frac{(\gamma+1)^2}{4\gamma}\right]^{\gamma(\gamma-1)}\left[\frac{4}{\gamma+1}\right]$$

Unfortunately, such panel methods do not provide approximations of the local surface heating, and hence, cannot be used for a full aerothermal analysis. Empirical correlations have historically been applied as correction factors to account for higher levels of fidelity but have not been explored in this work. As such, S/HABP has been used as an aero-only tool to analyze the aerodynamic performance of the structure pre- and post-distortion.

C. Coupling Approaches

A unique challenge to modelling FTSI is the coupling between individual physics solvers. The challenge with coupling solvers primarily includes the treatment of boundary conditions and disparity between the time scales of the physics. For example, the transient response of a hypersonic flow is typically on the order of microseconds whilst a thermal problem may require seconds to resolve. When considering chemically reacting flows, a time scale of nanoseconds or less must be considered. Hence, it becomes evident that updating a full multiphysics solution at the smallest time scale is a redundant and often impossible task. The use of a loosely coupled approach updates each solver at their own independent time scales whilst a tightly coupled approach updates all solvers at one unified scale. Furthermore, a reduction in computation time can also be achieved by considering the direction that information is passed.

In the event that deformation of a structure has little impact on the solution of a fluid field, boundary condition information can be passed one-way, wherein the deformation of a geometry is not passed back to the fluid solver. Ultimately, the job of an engineer is to consider the required levels of fidelity to achieve a suitably accurate solution in the most practical timeframe. A diagram showing two-way coupling between a fluid and structural solver is shown in Figure 5.

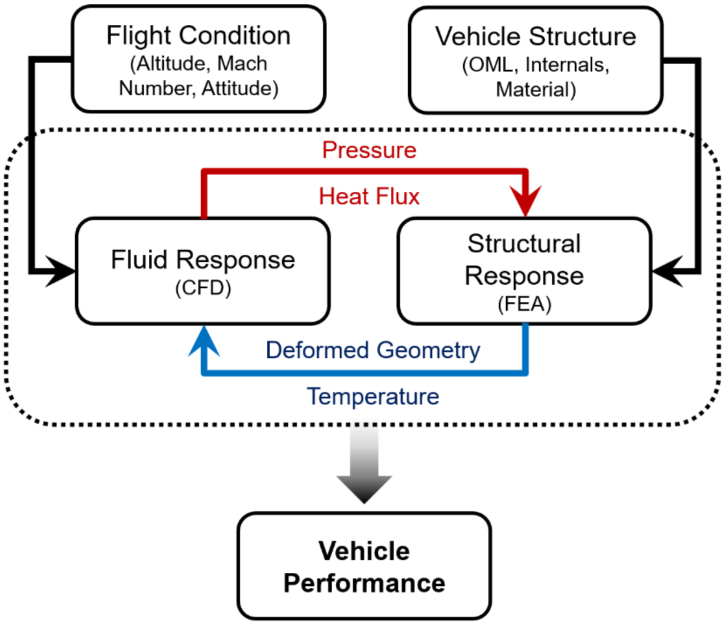

Figure 5. Two-way coupled fluid-thermal-structural interaction.

A final consideration for coupling approaches is how to handle the solution of the structure's temperature field. The simplest option is to obtain the wall-temperatures from the CFD solution and then interpolate throughout the internal structure. This approach requires *a priori* knowledge of the heat transfer and emissivity coefficients which may not always be accurate. The resulting temperature field likewise relies on the assumption that the interior structure is relatively uniform such that a linearly interpolated temperature (LIT) is reasonably accurate.

A higher-fidelity approach is to employ conjugate heat transfer (CHT) wherein the fluid solution is solved simultaneously with the temperature field of the structure. CHT demands more computational resources, can introduce instabilities, and requires greater consideration of the fluid-solid interface, but ultimately produces a much more accurate solution.

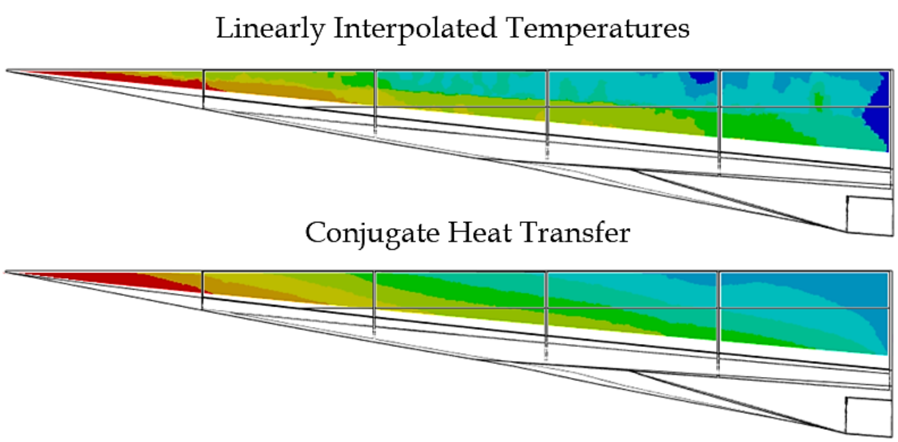

Figure 6. A qualitative comparison between LIT (top) and CHT (bottom) for the thermal soak through one of the vehicle's longerons.

Both the LIT and CHT approaches were attempted but due to the simple structure of the reference vehicle, it was ultimately decided that the LIT method provided reasonable results at significantly lower computational cost. A comparison of deformations obtained through one-way FTSI employing both approaches is shown in Figure 7. The presence of the structure within the CHT modelling creates a relieving effect due to the thermal mass. Hence, lower temperatures are typically observed and likewise, lower deflections are evident, particularly in regions of high heating.

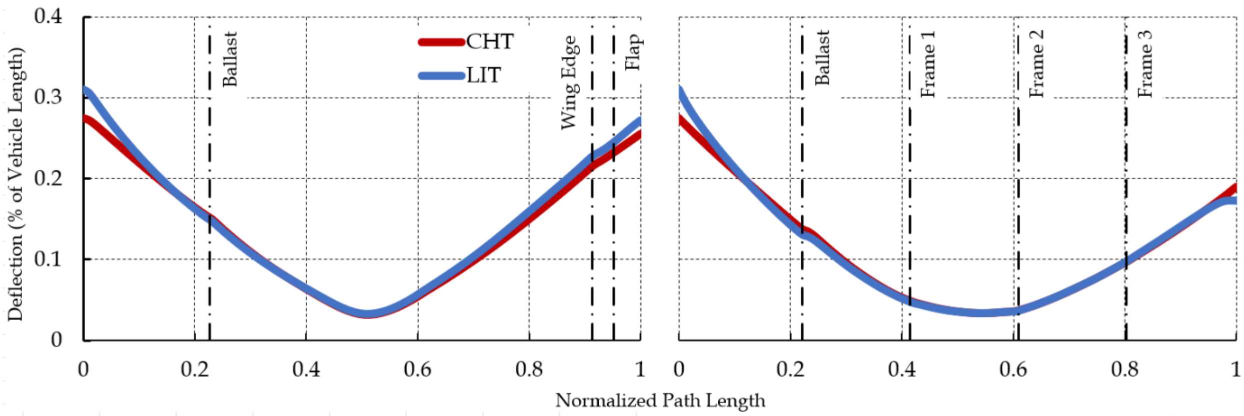

Figure 7. One-way deformations for LIT and CHT along the leading edge (left) and spine (right) of the vehicle.

IV. Results and Discussion

A. Undistorted Aerodynamics

The first aerodynamic database obtained for the reference vehicle was that for the undistorted aerodynamics. This can be considered as the baseline or nominal vehicle performance with an infinitely rigid structure. The vehicle exhibits favorable characteristics, including a modest maximum lift-to-drag ratio, which is of particular importance for gliding vehicles. A comparison between the reference vehicle and the empirical limits for a waverider, as obtained from Küchemann [37] and Bowcutt, et al. [38] is shown in Figure 8 below.

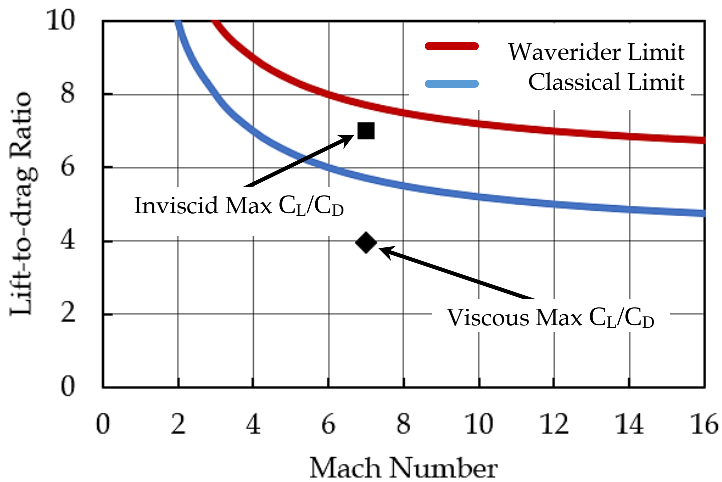

Figure 8. A comparison of lift-to-drag performance of the reference vehicle with theoretical limits.

Aerodynamic performance over the entire assessed envelope is shown in Figure 9. The reference vehicle demonstrates minimum drag at -3° angle of attack and a negative pitching moment coefficient slope, indicative of positively stable dynamics. Whilst positive stability is desirable for gliding conditions, this limits the maneuverability of the vehicle and hence, future considerations could be made to re-adjust the center-of-gravity to decrease stability and lessen the requirements of control surfaces. Maximum lift-to-drag (or glide) performance is obtained at a +3° angle-of-attack and is the optimum angle to maintain for maximum distance.

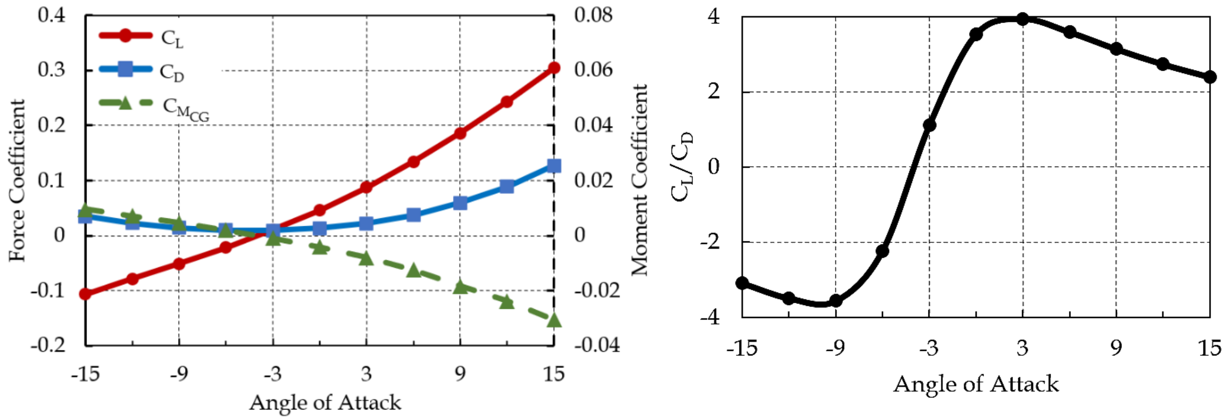

Figure 9. Undistorted aerodynamic performance of the reference vehicle at the given cruise condition.

A curve fit of the vehicle drag polar shown in Figure 10, reveals that the relationship can be well approximated with a quadratic of the form $C_D = C_{D_0} + KC_L^2$, with C_{D_0} representing the vehicle profile drag and K, the coefficient for all types of lift-induced drag. This simple relationship, more typically applied to subsonic aircraft can be employed to analyze the effects of aerothermal shape distortion on individual drag sources.

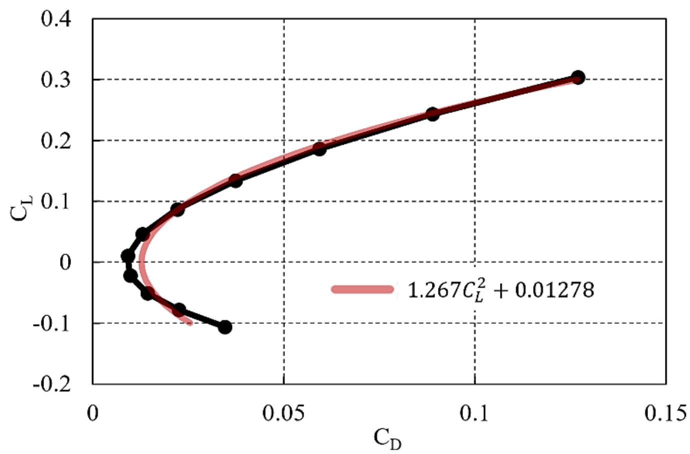

Figure 10. The reference vehicle's drag polar with quadratic curve fit.

Finally, a comparison is made between aerodynamic performance obtained using both the viscous SA model and the MN method. The application of a lower fidelity tool such as an inviscid panel method can be a very useful way to approximately verify data obtained from another source. It is expected, and evident, that the MN method tends to underpredict the drag on the vehicle whilst providing a reasonably good estimation of the lift.

Lift-to-drag performance achieved from the MN method is likewise much higher than the viscous values obtained from the SA model. The most critical distinction between the two sets of data, as shown in Figure 12, is that the angle-of-attack for maximum C_L/C_D is different in both cases. Hence, it is evident that whilst such inviscid methods provide a convenient and rapid assessment of aerodynamic performance, they should always be confirmed with a higher fidelity data source. Nonetheless, both sets of data tend to converge well at higher angles of attack as the slender waverider appears blunter to the freestream, and hence is dominated by inviscid forces. This result may be extrapolated to consider that inviscid panel methods would generally perform much better for blunter bodies, such as those designed for re-entry, as opposed to slender bodies designed for inter-atmospheric cruise or glide.

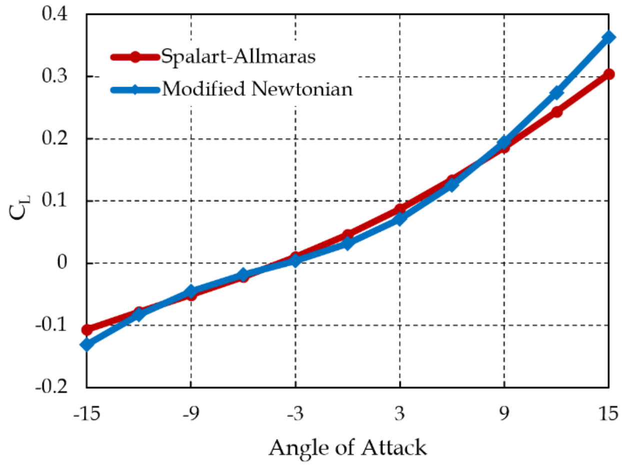

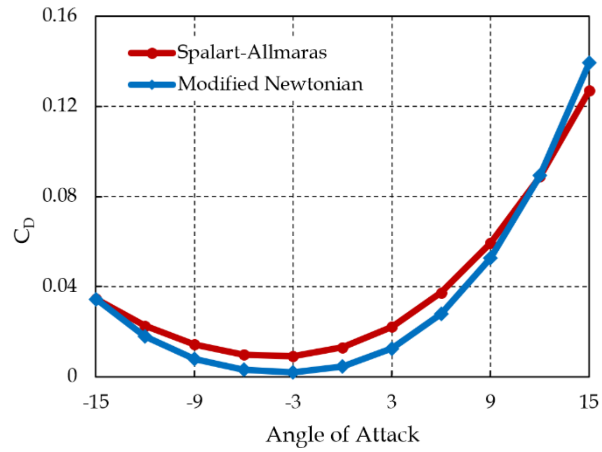

Figure 11. A comparison between the Spalart-Allmaras RANS model and the inviscid modified Newtonian model for computing undistorted aerodynamic performance.

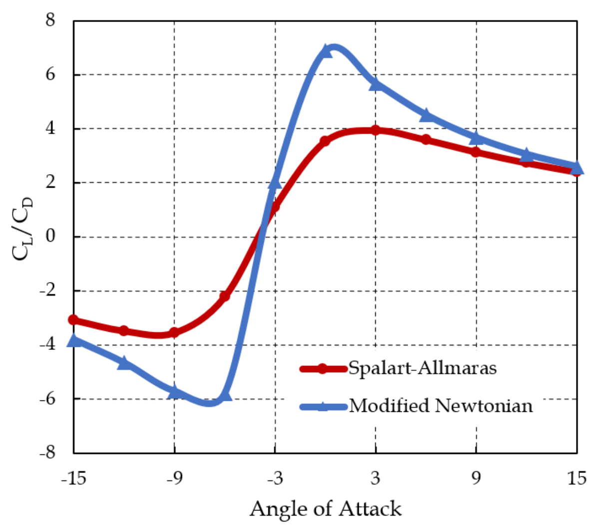

Figure 12. A comparison between lift-to-drag ratio computed from the Spalart-Allmaras RANS model and the inviscid modified Newtonian method.

An example of the temperature field of the vehicle is shown below in Figure 13 along with density gradient contours at different longitudinal stations. The temperature field is nominally as expected, the leading edge of the structure is considerably hotter than the remainder of the vehicle. Moreover, the tungsten ballast in the nose, being solid, and owing to its higher thermal conductivity, exhibits higher temperatures than the remainder of the structure. There should be significant design consideration given to the interface between the ballast and the structure where high thermal stresses are expected – particularly during transient heating. The plot of density gradient contours showcases how the majority of the leading edge shock is captured on the windward of the vehicle, thereby generating compression lift. There is some bleed at the leading edge from the windward to leeward sides which offers potential to further optimize the design.

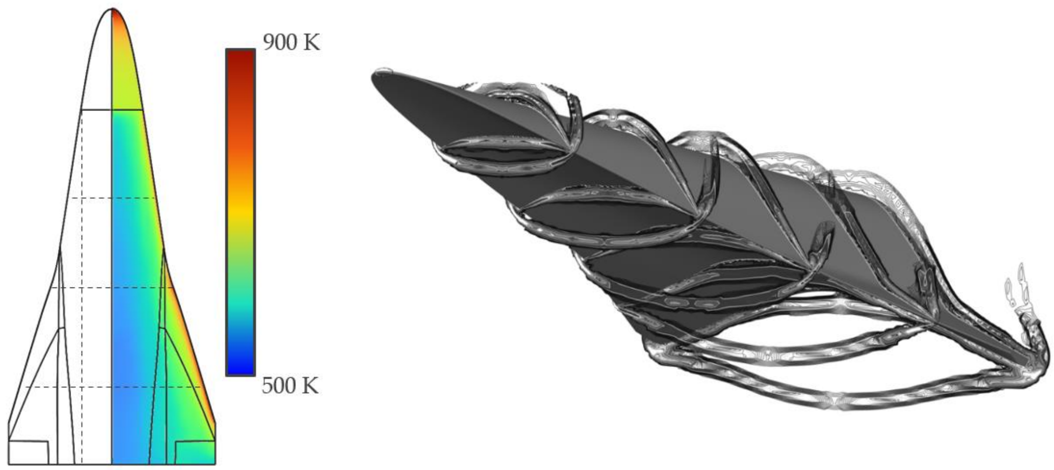

Figure 13. Temperature contours (left) and density gradient contours (right) for 0-degree AoA.

B. Distorted Aerodynamics

Aerodynamic performance of the aerothermally distorted vehicle is shown in Figure 14 and Figure 15. In all cases, two-way steady-state FTSI was performed with LIT until convergence was obtained. It can be clearly observed that the general trends in vehicle performance remain the same with the vehicle remaining positively stable. The largest deflections are observed at the bow and stern of the vehicle with some panel members beginning to bow, but the effect of this is not clear on changes in performance.

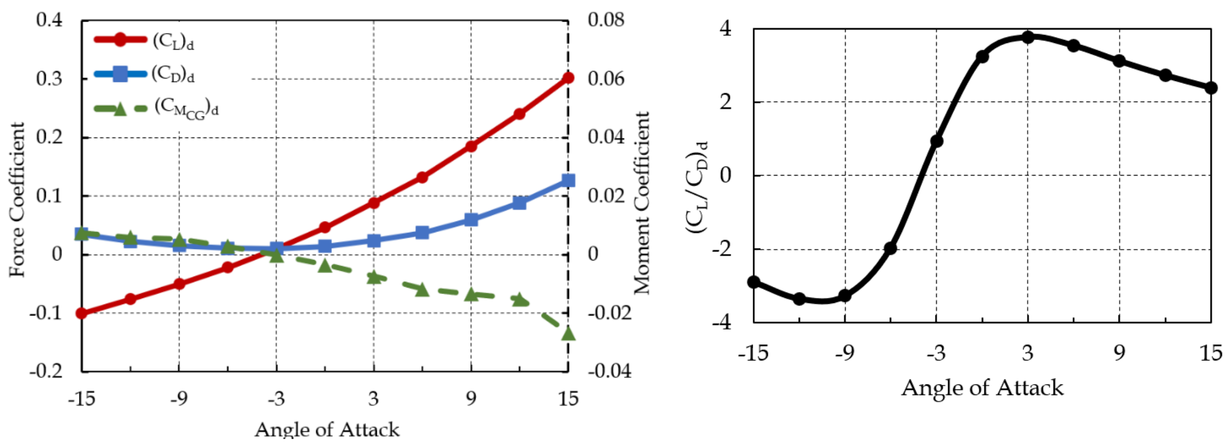

Figure 14. Distorted aerodynamic performance of the reference vehicle at the given cruise condition.

Ultimately, the aerothermally-distorted body results in a 13.4% increase in profile drag. The lift induced drag coefficient decreases slightly but is a potentially negligible result considering the uncertainty in curve fitting. The increase in profile drag indicates that aerothermal shape distortion significantly influences aerodynamic performance from changes in vehicle geometry and not from changes in flow physics. Deformation of the vehicle resulted in a 1.07% increase in frontal projected surface area, creating a blunter body that could explain the increase in profile drag. Furthermore, the 0.61% increase in total wetted surface area observed as a result of thermal expansion will result in greater skin friction and therefore an increase in total drag.

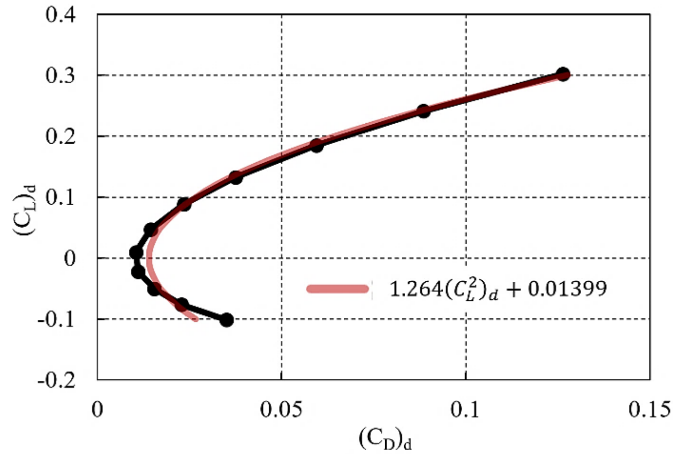

Figure 15. Distorted drag polar with curve fit.

Table 4. Comparison in drag polar curve fits.

	Undistorted	Distorted	Change (%)
Curve-Fit Profile Drag	0.01278	0.01399	+9.04%
True Profile Drag	0.00931	0.01065	+13.4%
Lift Induced Drag Coefficient	1.267	1.264	-0.24%

As observed in Figure 16, a maximum increase in drag and decrease in maximum lift-to-drag ratio of 14.8% and 16.2% can be observed respectively at -3° angle of attack. Lift coefficient generally decreases but does exhibit some minor increases at shallower angles of attack, likely owing to an increased body bluntness. Similarly, the effects of aerothermal shape distortion at higher angles of attack are less pronounced, owing to a similar body blunting effect. Drag coefficient demonstrates little change at comparably high angles of attack but lift suffers significant decreases. An anomalous change in lift coefficient occurs at -3° angle of attack, however, this is because the lift coefficient is approximately equal to zero at this attitude. Hence, any changes caused by aerothermal shape distortion have created a disproportionate change in lift when expressed as a percentage.

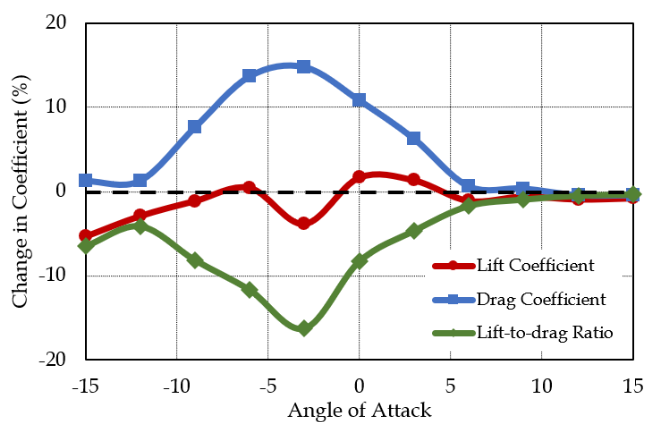

Figure 16. Percentage changes in aerodynamic performance at the cruise condition.

The nominal longitudinal static margin of the body, expressed as a percentage of the body length, likewise shows a reduction of 14.2%, indicating a decrease in the static stability of the vehicle due to aerothermal shape distortion. The nature of the deformed OML to vary depending on the angle-of-attack results in an attitude-dependent aerodynamic center, and hence, highly varying static margins and thus controllability and maneuverability.

Table 5. Nominal change in vehicle static margin.

	Undistorted	Distorted	Change (%)
Static Margin (%)	9.31	7.99	-14.2

Figure 17 provides a comparison of the pitching moment coefficient at the center-of-gravity for the entire alpha sweep between the undistorted and distorted vehicle. At higher angles of attack, the distorted vehicle exhibits significant changes in pitching moment coefficient. Such abrupt changes in stability limit the operational envelope of the vehicle, lest considerable effort is invested in developing technologies to counter the effects of distortion or control authority and effectiveness. A detailed study has not been conducted to understand the cause of such abrupt changes in performance and has been planned as an aspect of future work.

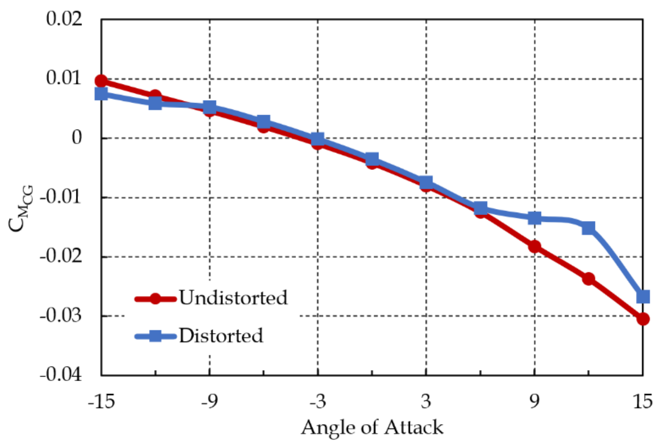

Figure 17. A comparison of pitching moment coefficient between the undistorted and distorted vehicle.

V. Conclusion

This work has explored the effects of aerothermal shape distortion upon a generic hypersonic waverider vehicle. The vehicle has been structurally under-designed to explore the effects that shape change has on the aerodynamic performance of such vehicle classes. Different methods for modelling the distortion phenomena, including the treatment of multiphysics coupling as well as levels of fidelity have been discussed. Overall, it is shown that the effects of aerothermal shape distortion result in noticeable changes to the aerodynamic performance of the vehicle. Such changes would result in radically different mission profiles than expected, and hence, consideration of such distortion is a key design parameter for hypersonic vehicles. Future work is currently being planned to expand this study to accommodate more realistic conditions including transient effects, larger control surfaces, and a more realistic internal structure. Experimental work will also being undertaken to validate the numerical predictions.

Acknowledgments

This research was supported by Lockheed Martin Australia. Any opinions, findings, and conclusions or recommendations expressed in this material are those of the authors and do not necessarily reflect the views of Lockheed Martin Australia. Numerical resources were provided by the National Computational Infrastructure (NCI) under the National Computational Merit Allocation Scheme (NCMAS).

References

[1] J. D. Anderson, *Hypersonic and high temperature gas dynamics*. AIAA, 2000.

[2] R. Wall, "Darpa Contemplates Hypersonic Spaceplane Demo," *Aviation Week & Space Technology,* vol. 157, no. 11, pp. 81-81, 2002.

[3] N. Viola, R. Fusaro, D. Ferretto, and V. Vercella, "Research, development and production costs prediction parametric model for future civil hypersonic aircraft," *Acta Astronautica,* vol. 204, pp. 58-72, 2023.

[4] R. H. Speier, G. Nacouzi, C. Lee, and R. M. Moore, *Hypersonic missile nonproliferation: hindering the spread of a new class of weapons*. Rand Corporation, 2017.

[5] R. Morgan *et al.*, "Impulse facilities for the simulation of hypersonic radiating flows," in *38th Fluid Dynamics Conference and Exhibit*, 2008, p. 4270.

[6] L. Trimmer, J. CARY, A, and R. Voisinet, "The optimum hypersonic wind tunnel," in *14th Aerodynamic Testing Conference*, 1968, p. 739.

[7] R. Savino, M. D. S. Fumo, D. Paterna, A. Di Maso, and F. Monteverde, "Arc-jet testing of ultra-high-temperature-ceramics," *Aerospace Science and Technology,* vol. 14, no. 3, pp. 178-187, 2010.

[8] R. Kimmel, D. Adamczak, K. Berger, and M. Choudhari, "HIFiRE-5 flight vehicle design," in *40th Fluid Dynamics Conference and Exhibit*, 2010, p. 4985.

[9] K. A. Damm, R. Gollan, and A. Veeraragavan, "Trajectory-Based Conjugate Heat Transfer Simulation of the BoLT-II Flight Experiment," in *AIAA SCITECH 2023 Forum*, 2023, p. 0292.

[10] T. Stathopoulos, "The numerical wind tunnel for industrial aerodynamics: Real or virtual in the new millennium?," *Wind and Structures,* vol. 5, no. 2_3_4, pp. 193-208, 2002.

[11] F. Liu *et al.*, "Surrogate-based aerodynamic shape optimization of hypersonic flows considering transonic performance," *Aerospace Science and Technology,* vol. 93, p. 105345, 2019.

[12] D. J. Dalle, S. M. Torrez, J. F. Driscoll, M. A. Bolender, and K. G. Bowcutt, "Minimum-fuel ascent of a hypersonic vehicle using surrogate optimization," *Journal of aircraft,* vol. 51, no. 6, pp. 1973-1986, 2014.

[13] A. R. Crowell, J. McNamara, and B. Miller, "Hypersonic aerothermoelastic response prediction of skin panels using computational fluid dynamic surrogates," *Journal of Aeroelasticity and Structural Dynamics,* vol. 2, no. 2, 2011.

[14] A. Dasgupta and J. Neely, "Fluid-Thermal-Structural Interactions on a Fin in Hypersonic Flow," in *Proceedings of the 19th Australasian Fluid Mechanics Conference*, 2014.

[15] N. J. Falkiewicz, C. E. Cesnik, A. R. Crowell, and J. J. McNamara, "Reduced-order aerothermoelastic framework for hypersonic vehicle control simulation," *AIAA journal,* vol. 49, no. 8, pp. 1625-1646, 2011.

[16] F. R. Chavez and D. K. Schmidt, "Analytical aeropropulsive-aeroelastic hypersonic-vehicle model with dynamic analysis," *Journal of Guidance, Control, and Dynamics,* vol. 17, no. 6, pp. 1308-1319, 1994.

[17] L. Pollock and G. Wild, "An initial review of hypersonic vehicle accidents," in *19th Australian International Aerospace Congress, Melbourne, Australia*, 2021.

[18] L. Pollock, A. K. Abdelwahab, J. Murray, and G. Wild, "The Need for Aerospace Structural Health Monitoring: A review of aircraft fatigue accidents," 2021.

[19] S. Bhattrai, L. McQuellin, G. M. Currao, A. Neely, and D. Buttsworth, "Influence of hypersonic fluid-structure interaction on the control authority of a trailing-edge flap," in *22nd AIAA International Space Planes and Hypersonics Systems and Technologies Conference*, 2018, p. 5265.

[20] L. Pollock and G. Wild, "Modal Analysis of a Scramjet Inlet for Optimization of Sensor Placement," in *ASCEND 2021*, 2021: American Institute of Aeronautics and Astronautics, in ASCEND, doi: doi:10.2514/6.2021-4084.

[21] S. Bhattrai, A. J. Neely, G. Currao, and L. P. McQuellin, "Impact of aeroelasticity on hypersonic intake performance," *International Soc. of Airbreathing Engines Paper ISABE-2019-24059, Canberra, Australia,* 2019.

[22] G. M. Currao *et al.*, "Hypersonic oscillating shock-wave/boundary-layer interaction on a flat plate," *AIAA journal*, 2021.

[23] P. B. Vasconcelos, L. McQuellin, K. Talluru, and A. Neely, "Hypersonic Fluid-Structure Interactions on a Compliant Clamped-Free-Clamped-Free Panel Under the Influence of Static Shock Impingement," in *AIAA SCITECH 2022 Forum*, 2022, p. 0241.

[24] Z. Tuten, A. J. Neely, B. R. Capra, K. M. Talluru, and L. P. McQuellin, "Design and Bench Testing of a Radiatively Heated Model for Hypersonic Fluid-Thermal-Structural Interaction Experiments," in *AIAA AVIATION 2022 Forum*, 2022, p. 3796.

[25] F. Zander, R. Morgan, U. Sheikh, D. Buttsworth, and P. Teakle, "Hot-wall reentry testing in hypersonic impulse facilities," *AIAA journal*, vol. 51, no. 2, pp. 476-484, 2013.
[26] T. A. Heppenheimer, *Facing the heat barrier: a history of hypersonics*. Government Printing Office, 2009.
[27] G. Collins, *Europe in Space*. Springer, 1990.
[28] J. Moran, L. McQuellin, L. Pollock, and A. Neely, "Wind-Tunnel based Free-Flight Testing of a Viscous Optimized Hypersonic Waverider," AIAA, 2023.
[29] L. P. McQuellin, A. Neely, and G. Currao, "Considerations for a Hypersonic Flight Test Investigating Fluid-Thermal-Structural Interactions," in *23rd AIAA International Space Planes and Hypersonic Systems and Technologies Conference*, 2020.
[30] U. S. Atmosphere, "National oceanic and atmospheric administration," *National Aeronautics and Space Administration, United States Air Force, Washington, DC*, 1976.
[31] R. Paciorri, W. Dieudonné, G. Degrez, J.-M. Charbonnier, and H. Deconinck, "Exploring the validity of the Spalart-Allmaras turbulence model for hypersonic flows," *Journal of Spacecraft and Rockets*, vol. 35, no. 2, pp. 121-126, 1998.
[32] B. S. Kirk, R. H. Stogner, P. T. Bauman, and T. A. Oliver, "Modeling hypersonic entry with the fully-implicit Navier–Stokes (FIN-S) stabilized finite element flow solver," *Computers & Fluids*, vol. 92, pp. 281-292, 2014.
[33] C. J. Roy and F. G. Blottner, "Assessment of one-and two-equation turbulence models for hypersonic transitional flows," *Journal of Spacecraft and Rockets*, vol. 38, no. 5, pp. 699-710, 2001.
[34] K. Kurbatskii and F. Montanari, "Application of pressure-based coupled solver to the problem of hypersonic missiles with aerospikes," in *45th AIAA Aerospace Sciences Meeting and Exhibit*, 2007, p. 462.
[35] V. Viti, V. Rao, and J. Abanto, "CFD simulations of super/hypersonic missiles: validation, sensitivity analysis and improved design," in *AIAA Scitech 2020 Forum*, 2020, p. 2123.
[36] F. P. Incropera, D. P. DeWitt, T. L. Bergman, and A. S. Lavine, *Fundamentals of heat and mass transfer*. Wiley New York, 1996.
[37] D. Küchemann, *The aerodynamic design of aircraft*. American Institute of Aeronautics and Astronautics, Inc., 2012.
[38] K. G. Bowcutt, J. D. Anderson Jr, and D. Capriotti, "Viscous optimized hypersonic waveriders," in *25th AIAA Aerospace Sciences Meeting*, (Aerospace Sciences Meetings: American Institute of Aeronautics and Astronautics, 1987.